

1

2 **A multiscale modelling framework of coastal flooding events for** 3 **global to local flood hazard assessments**

4 Irene Benito¹, Jeroen C.J.H. Aerts^{1,2}, Philip J. Ward^{1,2}, Dirk Eilander^{1,2}, and Sanne Muis^{1,2}

5 ¹Institute for Environmental Studies (IVM), Vrije Universiteit Amsterdam, The Netherlands.

6 ²Deltares, Delft, The Netherlands.

7 *Correspondence to:* Irene Benito (i.benito.lazaro@vu.nl)

8 **Abstract.** Tropical and extratropical cyclones, which can cause coastal flooding, are among the most devastating natural
9 hazards. Understanding coastal flood risk better can help to reduce their potential impacts. Global flood models play a key role
10 in this process. In recent years, global models and methods for flood hazard simulation have improved, but they still present
11 limitations to provide actionable information at local scales. One notable limitation is the insufficient resolution of global
12models to accurately capture the complexities of storms and topography of specific regions. Additionally, most large-scale
13hazard assessments tend to focus solely on either water level simulations or overland flooding, often relying on static flood
14modelling approaches. In this study, we introduce the MOSAIC modelling framework, a flexible Python-based framework
15designed to dynamically simulate both water levels and coastal flooding events. We use MOSAIC to simulate three historical
16storm events with the aim of assessing the effects of resolution in global models. MOSAIC's flexibility allows for the
17adjustment of both temporal and spatial model resolutions. Furthermore, its multiscale modelling approach allows to
18automatically generate and nest high-resolution local models within a coarser global model. This approach seeks to generate
19more accurate water levels, thereby enhancing coastal boundary conditions for dynamic flood modelling. Our findings indicate
20that the importance of model refinements is linked to the topography of the study area and the storm characteristics. For
21instance, refining temporal output resolution has a significant impact on small and rapidly intensifying tropical cyclones, but
22is less critical for extratropical cyclones. Additionally, the refinement of spatial output locations is particularly relevant in
23regions where water levels exhibit high spatial heterogeneity along the coast. In regions with complex topographies, grid
24refinement and higher-resolution bathymetry play a more significant role. While the validation from this study does not
25conclusively demonstrate that a specific refinement consistently yields better results, MOSAIC serves as a valuable resource
26for users to explore optimal settings tailored to their case studies and regions of interest, providing a bridge between fully
27global and fully local modelling approaches.

28 **1 Introduction**

29 Coastal flood events can have devastating impacts on societies, economies, and the environment when affecting densely
30populated and low-lying coastal areas (Wadey et al., 2015). Tropical cyclones (TCs) and extratropical cyclones (ETCs) are the
31cause of the most severe coastal flooding events (Douris et al., 2021; Dullaart et al., 2021; Haigh et al., 2016; UNDRR, 2020;
32Wahl et al., 2017). For example, Hurricane Harvey, in 2017, is one of the costliest storms in the United States' history, with
33an estimated damage of \$125 billion. Typhoon Idai, in Mozambique 2019, caused around 600 deaths and economic damages
34of \$770 million (Nhamo and Chikodzi, 2021; Sebastian et al., 2021). In 1953, an ETC was the cause of the most severe coastal
35flood event in Northwest Europe, resulting in more than 2000 deaths (Wadey et al., 2015). More recently, in 2010, ETC
36Xynthia hit the Atlantic coast of France, causing 47 deaths and €1.2 billion economic damages (CGEDD, 2010).

37 Coastal flood events are driven by extreme sea levels, resulting from a combination of mean sea level variations, tides, storm
38 surges and waves (Kirezci et al., 2020; Marcos et al., 2019; Vousdoukas et al., 2018a, 2017; Wahl, 2017). In recent years,
39 several studies have applied global hydrodynamic models to simulate coastal water levels (Dullaart et al., 2021; Muis et al.,
40 2016; Pringle et al., 2021; Vousdoukas et al., 2016a; Wang and Bernier, 2023). Subsequently, these water levels have been
41 used to derive extreme water level values for various return periods. These extreme water levels have then been used as input
42 into global overland flood models, and the resulting flood hazard maps have been used to assess flood exposure and risk
43 (Vousdoukas et al., 2016b). While these global studies have greatly improved our understanding of large-scale coastal flood
44 risks, they do not yet have the accuracy to provide actionable information about coastal flood events at local scales.

45 The accuracy of large-scale hazard assessments is limited by several factors related to the quality of the input data and
46 assumptions underlying the modelling approaches. Until now, the vast majority of large-scale hazard assessments have
47 primarily concentrated on either modelling extreme water levels or overland floods. However, each model component has its
48 own limitations. We identify here three main methodological limitations of large-scale hazard assessments. First, coastal
49 geometry strongly influences extreme sea levels (Bloemendaal et al., 2019; Dullaart et al., 2020; Mori et al., 2014; Woodruff
50 et al., 2023), with large variability at local scale. Consequently, in regions with complex morphologies, such as estuaries, semi-
51 enclosed bays or barrier systems, global models lack the resolution required to accurately resolve the extreme sea levels (Bunya
52 et al., 2010; Dietrich et al., 2010). Grid refinement and nesting of local high-resolution models within coarser global models
53 can result in improved coastal boundary conditions. Pelupessy et al. (2017) used a similar multiscale approach to obtain
54 realistic boundary conditions by nesting a global circulation model and a high-resolution barotropic model. Second, the
55 accuracy of input datasets such as the meteorological forcing and the bathymetry have large influence on the total water levels.
56 Coarse meteorological forcings – both in terms of spatial and temporal resolution – might not be able to capture the resolution
57 necessary to resolve intense storms, while errors in the bathymetric datasets will propagate to the modelling of storm surge
58 levels (Bloemendaal et al., 2019; Dullaart et al., 2020). Third, coastal flooding is a dynamic process where flood duration and
59 physical processes play a key role. However, given the high computational costs associated with using hydrodynamic flood
60 models, their use has been limited to local application. Most large-scale hazard assessments have used static flood modelling
61 methods, which neglect flood dynamics (Hinkel et al., 2014; Muis et al., 2016; Ramirez et al., 2016; Vafeidis et al., 2019;
62 Vousdoukas et al., 2016b). Additionally, large-scale hazard assessments typically focus on a single flood driver (Tiggeloven
63 et al., 2020; Vousdoukas et al., 2018b; Ward et al., 2020). However, TC and ETC events often produce precipitation, river
64 discharge, storm surges and waves, all of which can contribute to flooding. When these drivers occur in combinations, they
65 can significantly amplify flood hazards and risks. For instance, recent research showed that storm surge exacerbates fluvial
66 flooding at global scale (Eilander et al., 2020). Few studies have analysed the effects and interactions of multiple flood drivers.
67 While Bates et al. (2021) performed a combined risk assessment of fluvial, pluvial and coastal flooding for the continental
68 USA, Eilander et al. (2023) introduced the first globally-applicable compound flood modelling framework that accounts for
69 precipitation, river discharge and storm tides. However, the inclusion of waves in large-scale assessments and the interactions
70 between flood drivers remains a challenge.

71 In this study, we introduce the MOSAIC (MOdelling Sea Level And Inundation for Cyclones) modelling framework with the
72 aim of providing a flexible Python-based modelling framework that allows to dynamically simulate TC and ETC water levels
73 and coastal flooding events. To analyse the effects of model resolution, MOSAIC applies a multiscale modelling approach in
74 which local models with high-resolution (~45 m to 25 km) are nested within a large-scale model with a coarser resolution
75 (~2.5 km to 25 km). To enable hydrodynamic flood modelling, MOSAIC couples two existing modelling approaches: (1) to
76 simulate water levels generated from storm surges and tides at global to local scale it couples the hydrodynamic Global Tide
77 and Surge Model (GTSM) and Delft3D Flexible Mesh software; and (2) to dynamically simulate overland flooding at local
78 scale it couples the simulated water levels with the Super-Fast INundation of CoastS model (SFINCS). We use a reproducible

approach that is globally applicable and that can automatically generate local Delft3D Flexible Mesh models as well as local SFINCS models. In this study, we showcase the potential of the MOSAIC framework by applying it to three case studies where large storm surges caused catastrophic flooding events, namely historical storm events TC Irma, TC Haiyan, and ETC Xynthia (see Figure 1; Bertin et al., 2012; Cangialosi et al., 2018; Lapidez et al., 2015). For each of these storms, we simulate the coastal water levels and flood depths. Moreover, we perform a sensitivity analysis of different modelling settings with the goal of benchmarking model configurations with different resolutions.

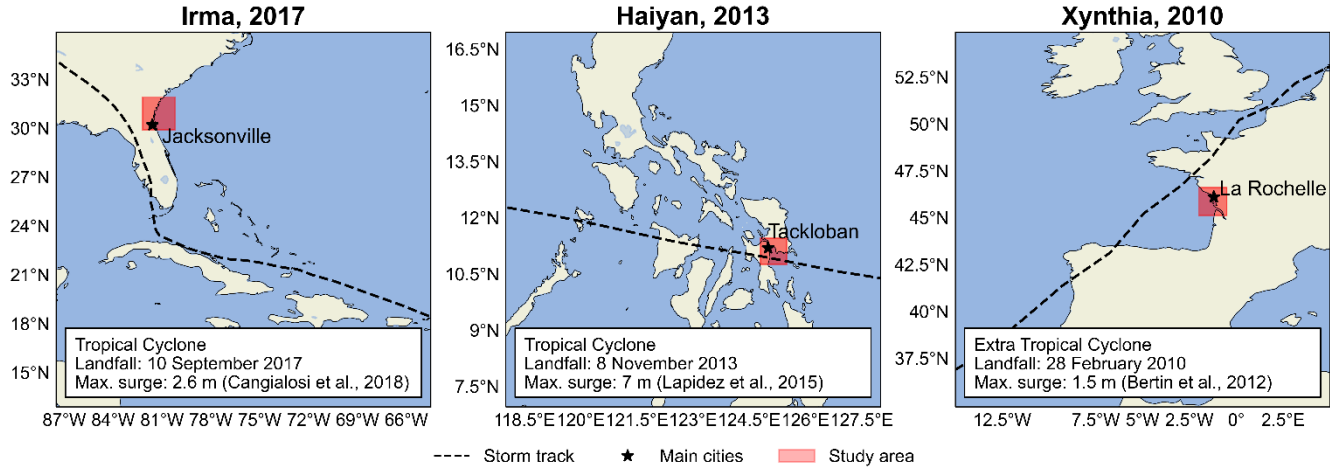


Figure 1. Case studies analysed on this paper. Left: Tropical cyclone Irma; middle: Tropical cyclone Haiyan; right: Extratropical cyclone Xynthia. The red area indicates the modelling domain of the flood analysis.

2 The MOSAIC modelling framework

The MOSAIC modelling framework, shown in Fig. 2, is a Python-based framework that integrates different packages, models and software. It consists of two main components: (1) the simulation of global coastal boundary conditions with the Global Tide and Surge Model (GTSM) (Section 2.1), including the dynamic downscaling with a local high-resolution model (Section 2.1.3); and (2) the overland flood hazard simulations using the SFINCS model (Section 2.2). Python scripts that enable adjustments to the GTSM settings are used to generate different model configurations. For the flood hazard simulations, MOSAIC uses the Hydro Model Tools (HydroMT) to prepare and postprocess SFINCS model input and output data.

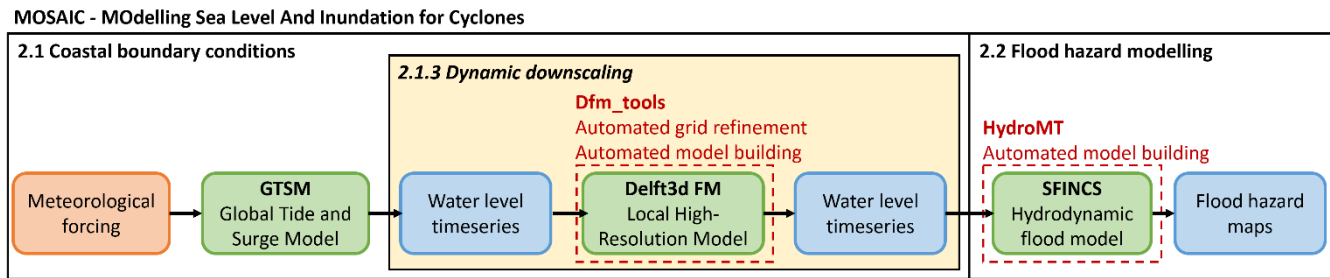


Figure 2. Flowchart showing the input (in orange), models (in green), outputs (in blue), Python packages (in red) and the optional dynamic downscaling feature (in yellow) of MOSAIC.

2.1 Derivation of coastal boundary conditions

2.1.1 Meteorological forcing

The meteorological forcing datasets used in this study vary per storm. For ETC Xynthia and TC Irma, we use mean sea level pressure and 10 m meridional and zonal wind components from the ERA5 re-analysis dataset at a horizontal resolution of 0.25 degrees and 1 hour temporal resolution (Hersbach et al., 2019). Because TC Haiyan is not well resolved in ERA5 (see Fig. A1), we use pressure and wind from tropical cyclone track data merged with ERA5. The tropical cyclone track data is retrieved

from the Joint Typhoon Warning Center at 6 hourly intervals (Naval Meteorology and Oceanography Command, 2022) and is converted to a polar grid with 36 radial bins, 375 arcs and a radius of 350 km using the Holland parametric wind model (Holland et al., 2010). Following the methodology of Dullaart et al. (2021) and Lin and Chavas (2012), we apply a counter-clockwise rotation angle of $\beta = 20^\circ$ and set the storm translation to surface background wind reduction factor at $\alpha = 0.55$. Additionally, we use an empirical surface wind reduction factor (SWRF) of 0.85 (Batts et al., 1980), and convert 1-minute average winds to 10-minute averages using a factor of 0.915 (Harper et al., 2010). The Holland model's output provides a file that defines a polar grid containing pressure and wind fields. To extend the pressure and wind fields beyond the Holland model's defined TC boundary, we linearly interpolate these fields on the outermost 75% to align with the ERA5 background data (Deltares, 2024).

2.1.2 Global storm surge and tide model

MOSAIC uses GTSMv4.1 to simulate total water levels resulting from tides and storm surges, ignoring baroclinic and wave contributions. GTSM is a global depth-averaged hydrodynamic model based on Delft3D Flexible Mesh (Kernkamp et al., 2011). It has a spatially-varying resolution of 25 km deep in the ocean and 2.5 km along the coasts (1.25 km for Europe) (Dullaart et al., 2020; Muis et al., 2020). The spatially-varying resolution makes it computationally efficient for simulating water levels at large scales. The bathymetry in the model is the 15 arcseconds resolution EMODnet bathymetry dataset for Europe (Consortium EMODnet Bathymetry, 2018), and the 30 arcseconds General Bathymetric Chart of Oceans 2019 dataset for the rest of the globe (GEBCO, 2014). Tides are generated internally with tide generating forces, while storm surges originate from external forcing with pressure and fields (Section 2.1.1; Muis et al., 2020). GTSM has been successfully validated using different meteorological datasets and has been shown to provide accurate extreme sea levels (Dullaart et al., 2020; Muis et al., 2020, 2016). Version 4.1 is a calibrated version of the model with also improved parametrizations for internal tides and bottom friction coefficient (Deltares, 2021; Wang et al., 2022). GTSM provides as output water level timeseries over a grid in the ocean and for locations along every ~5 km of the coast.

To validate the coastal component of our modelling framework, we compare total water levels from GTSM against observed total water levels from tide gauge stations of the Global Extreme Sea Level Analysis (GESLA) dataset (Haigh et al., 2023). This comparison is made for case studies where the GTSM output locations are found nearby tide gauge stations from GESLA (see Figure 3). GTSM output is referenced to mean sea level (MSL). We reference the GESLA water levels to the MSL by removing the annual average water level for each year, and subsequently removing the mean over the 1985-2005 period from the de-trended time series. To assess the accuracy of GTSM, we calculate the Pearson's correlation coefficient and the root mean-squared error (RMSE; see Table A1). Figure 4 and Fig. 5 show the time series of total water levels at different tide gauge stations during landfall of TC Irma and ETC Xynthia, respectively. The Pearson's correlation between the GTSM-simulated and observed total water levels is high for both events, indicating a good agreement. For TC Irma, the average correlation across the nine stations is 0.93 with a standard deviation of 0.06 m. For ETC Xynthia, the average correlation across the six stations is 1.00 with a standard deviation of 0.01. Additionally, TC Irma has a RMSE of 0.28 m with a standard deviation of 0.09 m, and ETC Xynthia has a RMSE of 0.22 m with a standard deviation of 0.08 m. This shows that while there are some minor differences between the GTSM simulations and observations, generally there is a good agreement.

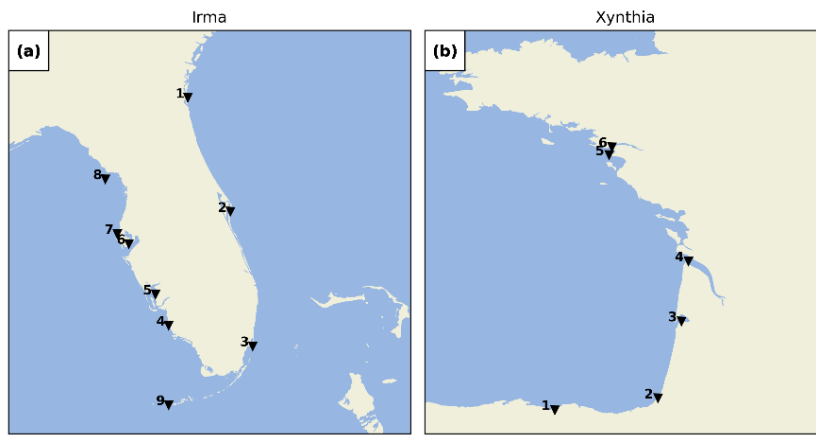


Figure 3. GESLA tide gauge stations for the case studies Irma (panel a) and Xynthia (panel b).

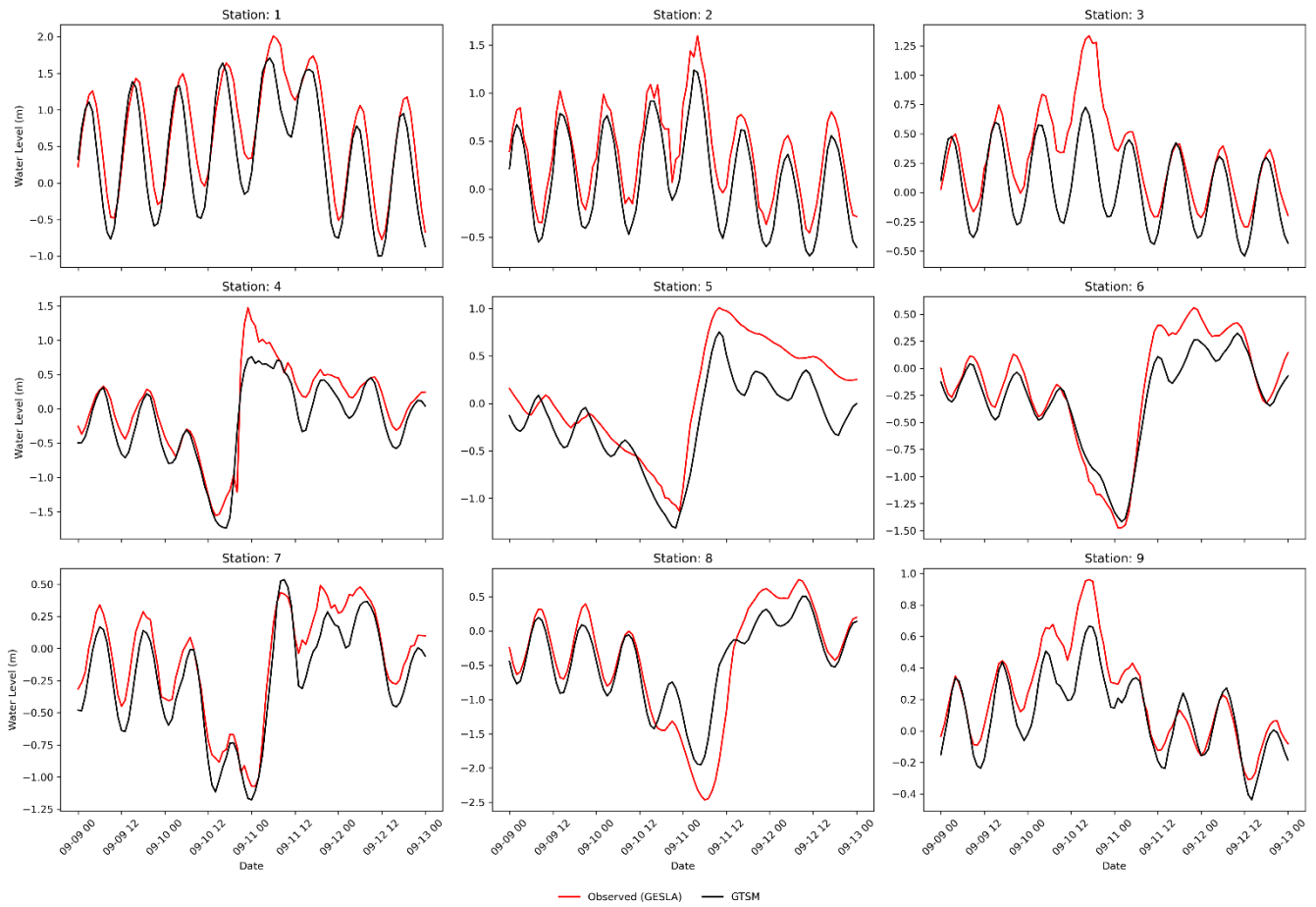


Figure 4. Validation of total water levels for the case study Irma, for the nine tide gauge stations depicted in Fig. 3.

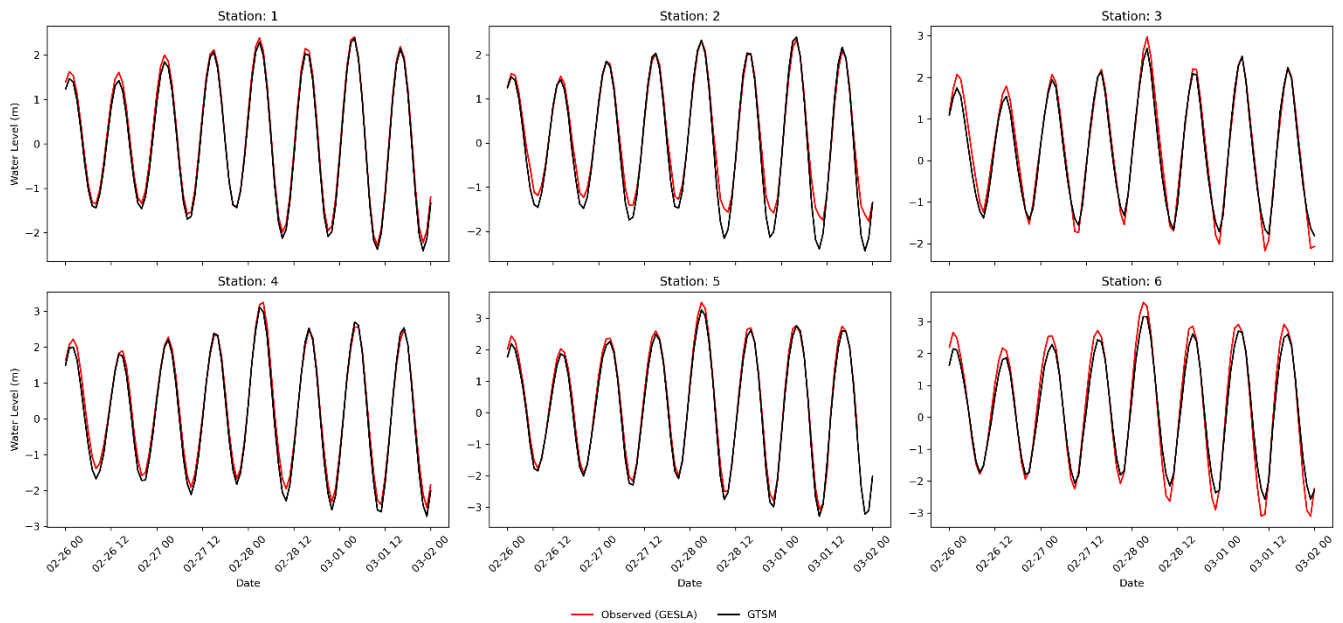


Figure 5. Validation of total water levels for the case study Xynthia for the six tide gauge stations depicted in Fig. 3.

2.1.3 Dynamic downscaling

The dynamic downscaling within MOSAIC consists of two parts. First, MOSAIC generates a local high-resolution model with Delft3D Flexible Mesh using the Python package `dfm_tools` (Veenstra, 2024). `Dfm_tools` allows to automatically create a local modelling grid with a spatially-varying resolution based on the specified maximum and minimum grid cell sizes as well as the Courant's number derived from the bathymetry data provided (Veenstra, 2024). The bathymetry of the local model can be updated by interpolating a new bathymetric dataset into the newly generated grid. The settings to automatically generate the local high-resolution models used in this study can be found in Section 2.3. Second, MOSAIC uses an offline coupling approach to nest the local Delft3D Flexible Mesh model within GTSM. A Python script is used to first identify the boundaries of the local Delft3D Flexible Mesh model. These boundaries are then used to determine the specific locations where GTSM output should be extracted. Subsequently, GTSM provides the water level timeseries at the boundaries of the local model. Finally, the local high-resolution model is executed using the water levels derived from GTSM as forcing input, together with the same meteorological forcing as for GTSM.

2.2 Hydrodynamic flood hazard modelling setup

MOSAIC uses the Super-Fast INundation of CoastS (SFINCS) model to simulate overland storm surge flood depths. SFINCS is a reduced-physics hydrodynamic model developed for a more computationally efficient dynamic flooding approach than full shallow water equation models (Leijnse et al., 2021). It solves simplified equations of mass and momentum, similar to the LISFLOOD-FP model (Bates et al., 2010). SFINCS has been successfully applied to model compound flooding for tropical cyclone Irma in 2017 (Eilander et al., 2023; Leijnse et al., 2021). Its modelling output results in similar results to those from full shallow water equation models, while reducing computational expenses by a factor of 100 (Leijnse et al., 2021). To speed up the flood model simulations, we use the subgrid schematization from SFINCS for all the simulations (Leijnse et al., 2020).

For this study, we use GEBCO 2020 (15 arc seconds spatial resolution; (Weatherall et al., 2020)) as input dataset for the bathymetry and FABDEM (30 m spatial resolution; (Hawker et al., 2022)) as input dataset for the land elevation. Except for ETC Xynthia. For ETC Xynthia we use the 5 m resolution LiDAR-based DEM developed by the French National Geographic Institute (IGN) because it better represents dikes in the region, leading to better flood estimates than FABDEM (see Fig. A8). The spatially varying roughness coefficients used within SFINCS are derived from the land use maps of the Copernicus Global Land Service (Buchhorn et al., 2020). Within MOSAIC, SFINCS is coupled offline with water levels from GTSM at 1-hourly

172 resolution for the default settings. The Mean Dynamic Topography (DTU10MDT; (Andersen and Knudsen, 2009) is used to
 173 convert the vertical reference of the water levels from mean sea level to the EGM2008 geoid. The resulting flood hazard maps
 174 have a resolution of 30 m.

175 To build the SFINCS models and couple them with GTSM, MOSAIC uses the HydroMTv0.7.1 (Hydro Model Tools) package
 176 (Eilander et al., 2023). HydroMT is an open-source Python package, which provides automated and reproducible model
 177 building and analysis of results. HydroMT uses a modular approach in which datasets and model setup configurations can
 178 easily be interchanged. In the MOSAIC framework presented in this paper, we take advantage of HydroMT in several ways:
 179 (1) to automatically convert the forcing files from GTSM and the other input into the model specific input format; (2) to easily
 180 build a reproducible SFINCS model; and (3) to perform the analysis of the SFINCS model output. SFINCS is forced with
 181 GTSM water level timeseries at locations along every ~5 km of the coastline, and provides as output water level timeseries for
 182 each grid cell. Finally, flood depth maps are derived from the maximum water levels by subtracting the DEM.

183 To validate the hydrodynamic flood hazard modelling component of the modelling framework, we compare the modelled flood
 184 extents with observed flood extents derived from field measurements. This comparison is done for Xynthia, the only case study
 185 for which observed flood extent data are available (Breilh et al., 2013; DDTM, 2011). We measure the model skill using: (1)
 186 the hit rate (H), defined as the flood area correctly simulated over the observed flooded area (Eq (1)); (2) the false-alarm ratio
 187 (F), defined as the area wrongly simulated over the observed flooded area (Eq (2)); and (3) the critical success index (C),
 188 defined as the area correctly simulated to be flooded over the union of the observed and modelled flooded area (Eq (3)). Figure
 189 6 shows the skill of the modelled maximum flood extents by SFINCS using the GTSM water levels as forcing. The hit rate is
 190 0.78, correctly representing the flooding in most regions, only underestimating it in regions further inland. The false-alarm
 191 ratio of the model is 0.62. Flooding is overestimated in the north, likely due to the lack of flood protection measures included
 192 in the model that are present in reality. The critical success index is 0.48, as a result of the areas well simulated and those over
 193 and underpredicted. While the performance of the flood model is negatively affected by the quality of the topography and the
 194 representation of local features such as dikes, we consider the performance sufficient for large-scale modelling and comparable
 195 to other studies such as Ramirez et al. (2016) and Vousdoukas et al. (2016b).

$$196 \quad H = \frac{F_{\text{modelled}} \cap F_{\text{observed}}}{F_{\text{observed}}} \quad (1)$$

$$197 \quad F = \frac{F_{\text{modelled}} / F_{\text{observed}}}{F_{\text{observed}}} \quad (2)$$

$$198 \quad C = \frac{F_{\text{modelled}} \cap F_{\text{observed}}}{F_{\text{modelled}} \cup F_{\text{observed}}} \quad (3)$$

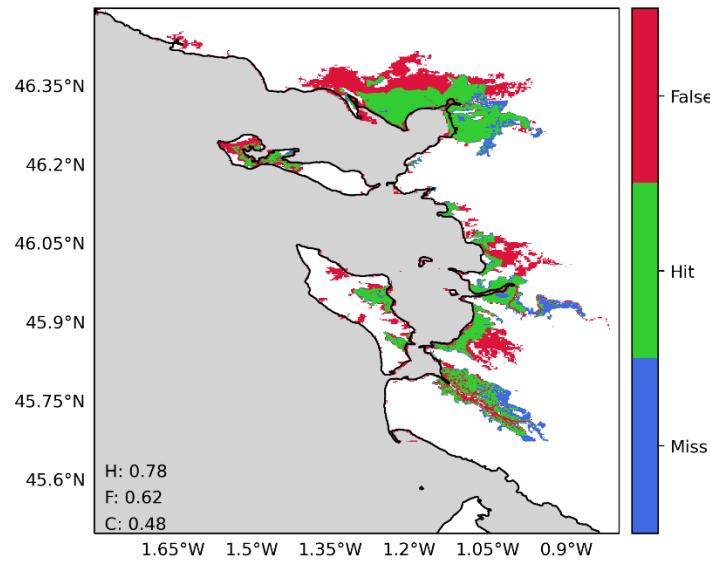


Figure 6. Validation of the flood hazard modelling component of the modelling framework for the case study Xynthia, using the water levels of the default configuration of GTSM as a forcing. The maps compare the modelled and observed maximum flood extents, where: green indicates flood areas correctly simulated; blue flood areas not simulated but observed; and red flood areas simulated but not observed. Performance indicators for the hit rate (H), false-alarm ratio (F) and critical success index (C) are shown in each panel.

2.3 Sensitivity analysis

Using the MOSAIC modelling framework, we analyse the effects of refining the resolution of GTSM on the simulated water levels and assess how these propagate into the results for the flood hazard simulated by SFINCS. As described in Table 1, we categorise model configurations in two distinct groups. The first group, which contains the global model configurations (G), includes the default model configuration (G1) and configurations that modify only the global GTSM model (G2 and G3). In this group, the refinements applied are: (1) the temporal output resolution, which is different than the implicitly calculated simulation timestep of GTSM, is refined from 1-hourly to 10-minute, allowing to capture more changes in water levels, including the peaks of the water levels (G2); and (2) the spatial output resolution is refined from locations along the coast every ~5 km to ~2 km, providing more coastal boundary conditions for the hydrodynamic flood hazard model (G3). The second group, which contains the nested model configurations (N), includes those model configurations that use a nested local model within the global model GTSM by performing dynamic downscaling. These model configurations include: (1) the nesting of local high-resolution models with refined grids into GTSM (N1); and (2) the nesting of local high-resolution models with refined grids and updated bathymetry into GTSM (N2). Finally, we evaluate the combined effects of all these refinements through the “fully refined” configuration (N3), which integrates both the enhanced temporal and spatial resolutions as well as the nested high-resolution models and updated bathymetry. The validation of GTSM and SFINCS shows sufficient performance for all the model configurations from Table 1 and Fig. 7 (see Table A1 and Figs. A2, A3 and A9).

221 **Table 1. GTSM model configurations used in the sensitivity analysis.**

| Model configuration | Nomenclature | GTSM grid resolution | Bathymetry | Spatial output resolution | Temporal output resolution |
|--|--------------|----------------------|----------------|---------------------------|----------------------------|
| Default configuration | G1 | ~25 to 2.5/1.25km | GEBCO2019 * | Original (~5 km) | 1h |
| Refined temporal output resolution | G2 | ~25 to 2.5/1.25km | GEBCO2019 * | Original (~5 km) | 10min |
| Refined spatial output | G3 | ~25 to 2.5/1.25km | GEBCO2019 * | Refined (~2 km) | 1h |
| Dynamic downscaling (Refined grid) | N1 | ~25 to 0.45km | GEBCO2019 * | Original (~5 km) | 1h** |
| Dynamic downscaling (Refined grid + Updated bathymetry) | N2 | ~25 to 0.45km | GEBCO2023 | Original (~5 km) | 1h** |
| Fully refined configuration | N3 | ~25 to 0.45km | GEBCO2023 | Refined (~2 km) | 10min** |

222 * EMODnet2018 for Europe (Xynthia case study)

223 **For the model configurations N1, N2 and N3, the temporal output resolution is also the temporal resolution of the coupling between
224 GTSM and the local high-resolution model.

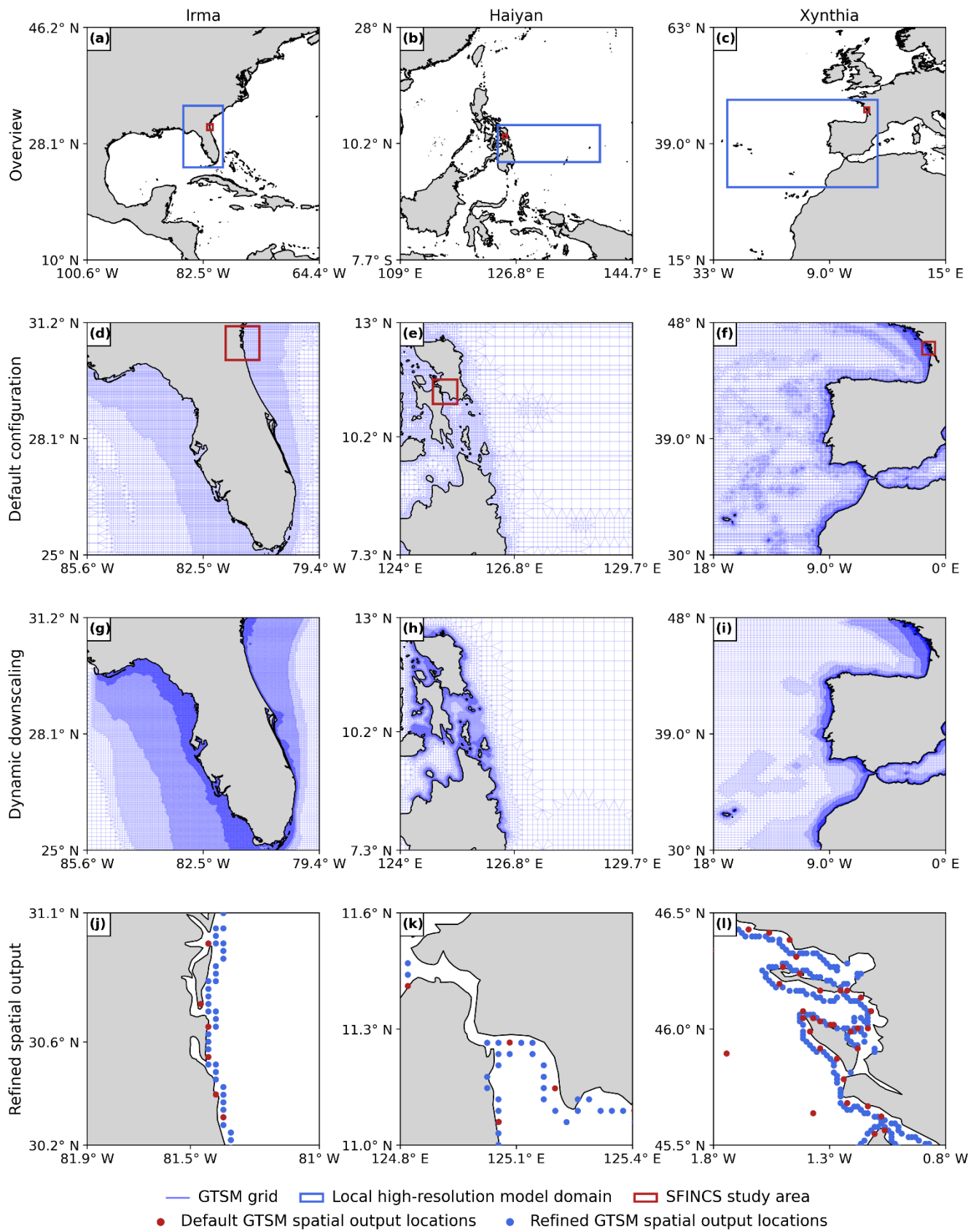


Figure 7. Overview of the model domains for the local high-resolution model and SFINCS, for the three case studies (panels a, b, c); default GTSM grid zoomed in (d, e, f); local high-resolution model grid zoomed in (g, h, i) and; GTSM spatial output locations for the default configuration and the refined spatial output configuration, zoomed into the SFINCS study area (j, k, l).

230 3 Sensitivity analysis of the model results

231 3.1 Multiscale storm surge modelling

232 Figure 8 panels a, e and i show the maximum water levels simulated by G1 for the three case studies, and depict the maximum
233 observed water levels for various GESLA tide gauge stations. To understand the effect of each individual refinement in the
234 maximum total water levels, Figure 8 presents the differences in maximum water levels between each refinement and the
235 model configuration G1. Figure 9 presents the differences in maximum water levels between the fully refined model
236 configuration N3 and the model configuration G1.

237 3.1.1 Effects of higher resolution on total water levels

238 Figure 8 panels b, f, j show that the refinement of temporal output resolution of GTSM from 1-hourly to the 10-minute intervals
239 of G2 results in higher maximum water levels across the entire model domain for all three case studies. For TC Irma (Fig. 8
240 panel b), the sensitivity of the water levels to the temporal refinement is relatively small, less than 10 cm. The small effect of
241 the temporal refinement for TC Irma can be observed as well in Table A1 and Fig. A2, where G1 and G2 present similar
242 timeseries and performance coefficients when compared to observed water levels. For TC Haiyan (Fig. 8 panel f), the
243 sensitivity of the water levels is significant. Water levels increase due to the temporal refinement up to 2 m along the coastlines
244 where TC Haiyan made landfall, showing that 1-hourly resolution is too coarse to accurately capture the water level response.
245 The cause for this is that TC Haiyan had a rapid intensification, and when modelling water levels at 1-hourly resolution we
246 overlook the storm's peak, resulting in an underestimation of the maximum water levels. G2 however, can capture the peak of
247 TC Haiyan more precisely (see Figs. A4 and A5). For ETC Xynthia (Fig. 8 panel j), the sensitivity of the water levels to the
248 temporal refinement is relatively small, less than 10 cm on average, and slightly higher in enclosed basins and estuaries near
249 La Rochelle. The small changes in water levels for ETC Xynthia are due to the inherent characteristics of ETCs, which typically
250 have larger dimensions, lower intensity, and a slower rate of intensification compared to TCs. This means that the changes in
251 water levels can be well captured at a 1-hourly resolution. The small effect of the temporal refinement for ETC Xynthia can
252 be observed as well in Table A1 and Fig. A3, where G1 and G2 present similar timeseries and performance coefficients when
253 compared to observed water levels.

254 The model configuration G3, where the spatial output resolution is refined, is not shown in Fig. 8 because increasing the
255 number of water level locations does not change the water level values themselves. However, this refinement becomes
256 significant when these values are applied as coastal boundary conditions to SFINCS (see Section 3.2.1), as a greater number
257 of coastal boundary conditions offer additional information for the flood model.

258 3.1.2 Effects of dynamic downscaling with original bathymetry on total water levels

259 Figure 8 panels c, g, k show that the model configuration N1 results in significant changes in water levels for all case studies.
260 The largest differences occur along the coasts, where the largest changes in model grid size resolution occur. For TC Irma
261 (Fig. 8 panel c), the nesting of a local model at high-resolution with GEBCO2019 results in maximum water levels that are up
262 to 0.3 m higher than G1 in the southwest of Florida, and up to 0.1 m lower in the southwest. These changes are caused by the
263 refined grid resolution in those regions in comparison to G1, which allows us to better resolve complex topography around the
264 barrier islands. Water levels for nine tide gauge stations along the coast indicate that while G1 underestimates the peak of TC
265 Irma in most locations (Fig. A2, all stations but station 7), N1 simulates on average higher peaks, resulting sometimes in
266 overestimations (Fig. A2, station 9). Additionally, the performance of N1 is slightly better than G1 for six tide gauge stations
267 (stations 1-6), as reflected in Table A1, which shows lower RMSE values. However, for stations 7-9, G1 shows slightly higher
268 RMSE and Pearson's correlation. For TC Haiyan (Fig. 8 panel g), the differences in maximum water levels are up to 1 m
269 higher than G1 near the landfall regions. These differences occur due to the refinement of the grid from 2.5 km to 45 m, which
270 results in a significant increase in the number of model grid cells that define regions of shallow bathymetry, especially around
271 the bay near Tacloban, resulting in a more detailed representation of water levels in that region. Thanks to the increase on grid

cells, the strait north of Tacloban for N1 is defined with multiple grid cells in comparison to the two grid cell width of G1 (see Fig. A6). Therefore, in that region N1 allows us to better resolve the topography of the region, and water can travel more easily northwards. For ETC Xynthia (Fig. 8 panel k), the water levels from the nested local model at high-resolution are overall lower than water levels for the G1. Near La Rochelle, those water levels are up to 0.2 m lower. When comparing the performance of N1 with G1 (Table A1 and Fig. A3), both model configurations can predict the timeseries pattern well, with high Pearson's correlation coefficients. Overall, the RMSE for Xynthia is similar for most tide gauge stations, except for two stations located in the mouth of estuaries (stations 3 and 6).

3.1.3 Effects of dynamic downscaling with updated bathymetry on total water levels

Figure 8 panels d, h, l show that the model configuration N2 results in relatively large changes in the water levels for all the case studies. The largest differences occur along the coasts and provide figures similar to those from N1. For TC Irma (Fig. 8 panel c), the nesting of a local model at high-resolution with updated GEBCO2023 bathymetry results in maximum water levels that are 0.3 m higher than G1 in the south of Florida. Compared to N1, model configuration N2 provides slightly higher water levels south of Florida. Those differences come from differences between GEBCO2023 and GEBCO2019 in the region. N2 shows a similar performance to G1 and N1 across nine tide gauge stations (Table A1 and Fig. A2). For TC Haiyan (Fig. 8 panels h), the differences in maximum water levels are up to 1 m higher than G1 at the landfall regions. Compared to N1, N2 provides on average higher maximum water levels, except in the bay of Tacloban where N1 presents on average higher maximum water levels. These differences come from the differences in GEBCO2019 and GEBCO2023. For ETC Xynthia (Fig. 8 panels l), the water levels from the nested local model at high-resolution with GEBCO2023 are lower overall than water levels for G1. Compared to N1, the model configuration N2 provides a similar pattern of water level decrease, however, the maximum water level reduction compared to G1 is slightly less than for N1. The performance of N2, as shown in Table A1 and Fig. A3, is comparable to that of G1 and N1, except at two tide gauge stations (station 3 and 6) where GEBCO2023 does not accurately capture the bathymetry of the river channels in the estuaries. In contrast, EMODNET2018, the bathymetry used in model configurations N1 and N3, better resolves these details (see Fig. A7).

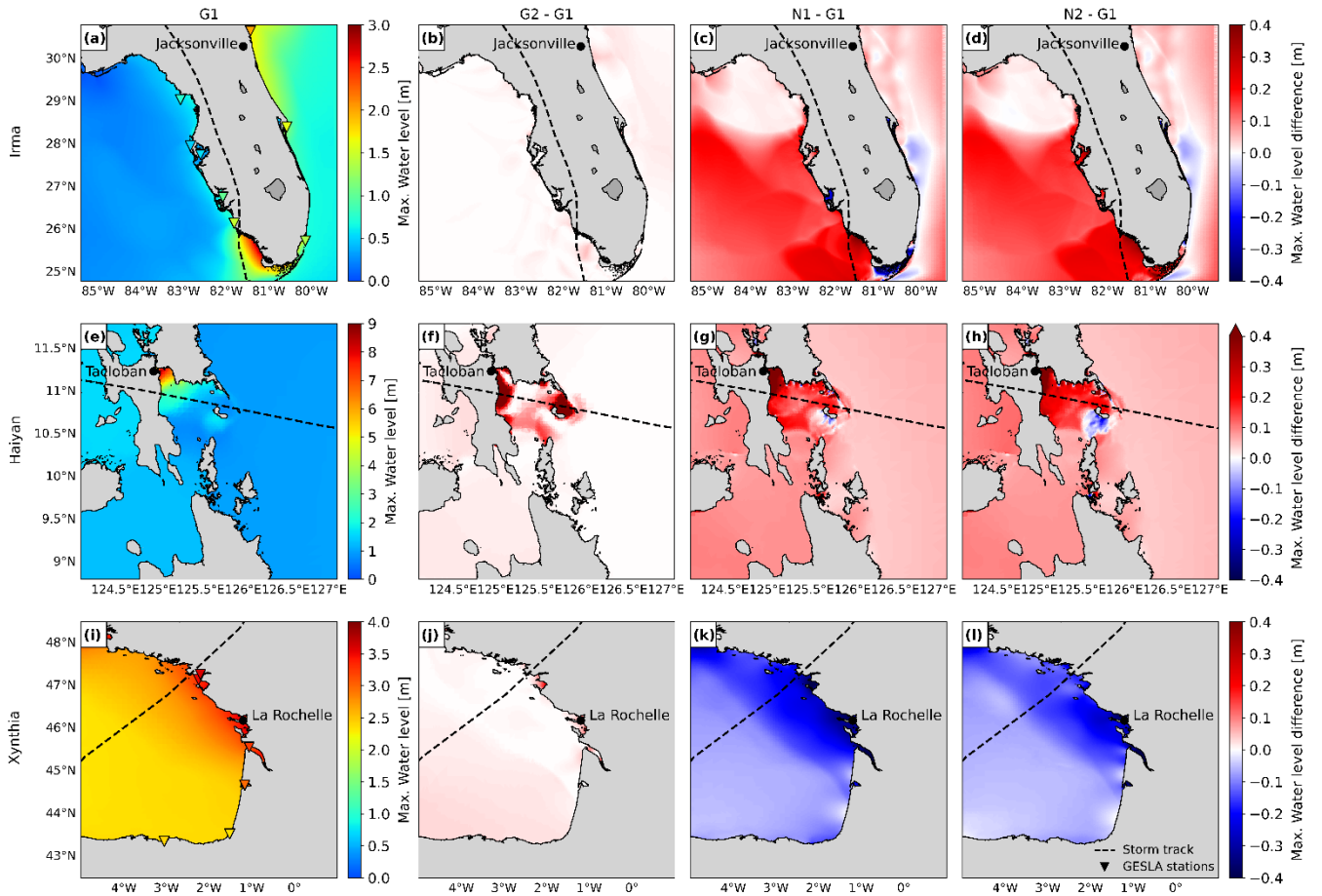


Figure 8. Maximum water levels for the three case studies for G1 (panels a, e, i). Difference between the maximum water level for each specific model configuration (see Table 1) and G1. Panels a, e, i show observed maximum water level from tide gauge stations of GESLA. Difference in water levels for G2 (panels b, f, j), N1 (panels c, g, k) and N2 (panels d, h, l).

3.1.4 Effects of a fully refined model on total water levels

In Fig. 9 we observe that the maximum waterlevel differences between N3 and G1 lead to significantly different results for each case study. For TC Irma N3 provides higher maximum waterlevels throughout almost the whole the domain, resulting in a picture similar to N2 but with higher water levels along the southeast coast. The maximum differences in maximum water levels between N3 and N1 are up to 0.3 m. For TC Haiyan N3 provides maximum water levels that resemble a combination of G2 in the regions where temporal refinement is relevant, and N2 in the rest of the study area. The differences between N3 and G1 in maximum waterlevels for Haiyan are more than 2 m in the coast near Tacloban. Finally, for ETC Xynthia N3 provides slightly higher maximum water levels in the south of the domain compared to G1, where the effects of G2 predominate, and lower maximum water levels in the north, where the effects of N2 are more dominant.

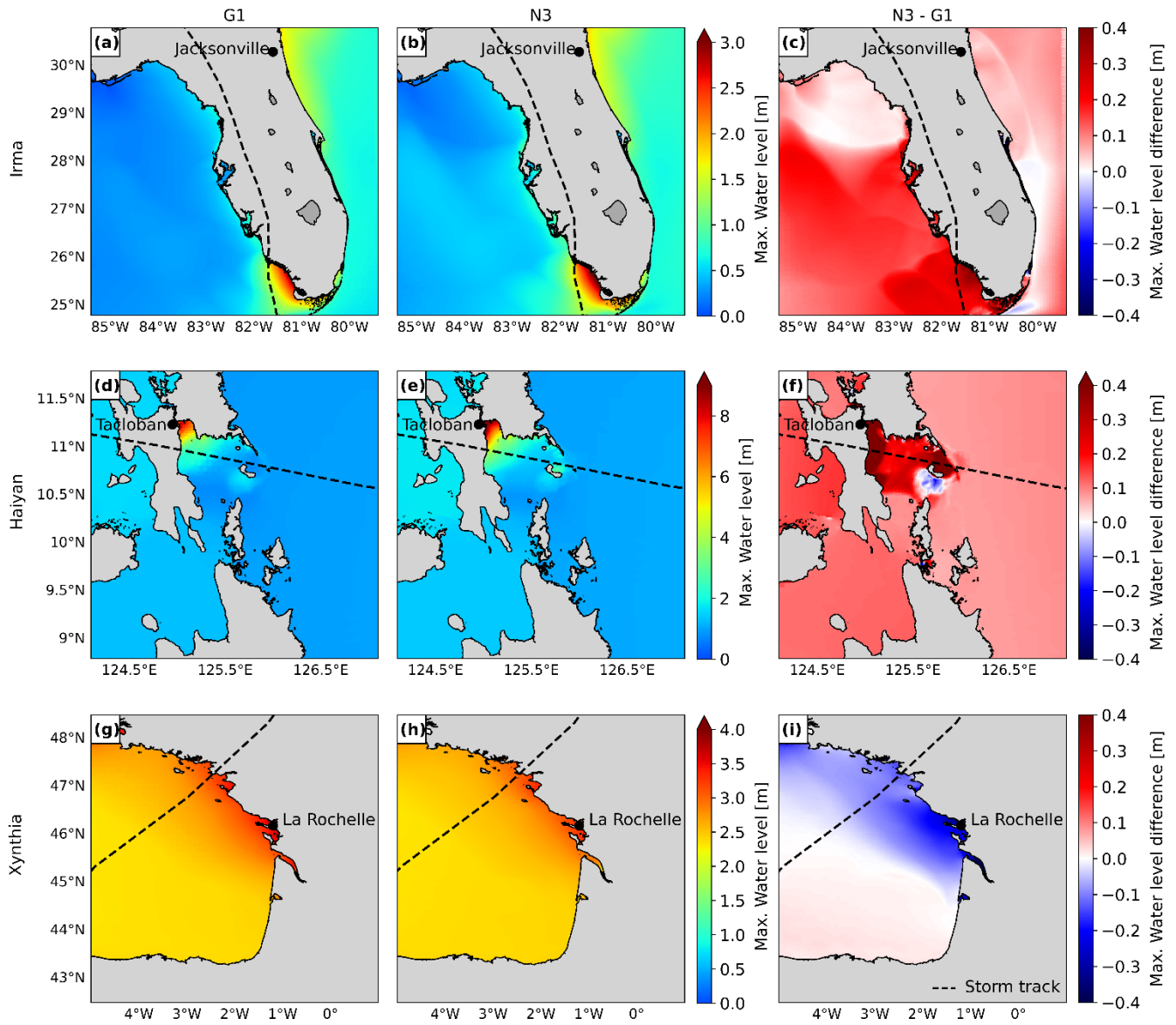


Figure 9. Maximum water levels for the three case studies, for the default configuration G1 (panels a, d, g) and for the fully refined configuration N3 (panels b, e, h). Difference between the maximum water level for N3 model configuration and G1 (panels c, f, i).

3.2 Hydrodynamic flood modelling

As a second step in the sensitivity analysis, we analyse how the effects of the different storm surge model configurations propagate to the SFINCS flood model. In Figure 10 we compare the maximum flood depths of each refinement and G1. Figure 11 shows the maximum flood depth differences between N3 and G1.

3.2.1 Effects of higher resolution on flood depths

Figure 10 panels b, g, l show that the refinement of GTSM's temporal output resolution from 1-hourly to 10-minute intervals of G2 provides different results for each case study. For TC Irma (Fig. 10 panel b), the small increase in water levels as a result of the temporal output refinement (Section 3.1.1) also results in a small increase in flood depths. Conversely, TC Haiyan (Fig. 10 panel g) experiences much higher water levels along the coast at higher temporal resolution. As a result, it also experiences significantly higher flood depths, surpassing G1 by 1m in regions near Tacloban. ETC Xynthia (Fig. 10 panel l) experiences an increase in water levels along the coast for the 10-minute temporal output resolution, especially in the study region of SFINCS. This results in an increase in flood depths of up to 0.1 m. For ETC Xynthia, G2 shows a higher hit rate and false-alarm ratio compared to G1, but the same critical success index (see Fig. A9).

Figure 10 panels c, h, m show that refinement of the spatial output locations of G3 provides coastal boundary conditions to SFINCS at additional locations, thereby providing more water level input to the flood model. panel c shows that this refinement results in lower flood depths north and around Jacksonville for TC Irma. Conversely, for TC Haiyan (Fig. 10 panel h), the increase in spatial inputs results in higher flood depths in most of the study area, particularly exceeding more than 1 m the G1 flood depths around Tacloban. For ETC Xynthia (Fig. 10 panel m) the refinement of spatial water level inputs leads to higher flood depths north of La Rochelle of up to 0.1 m, while south of La Rochelle there are barely any changes compared to G1. For ETC Xynthia, G3 shows the same hit rate as G1, higher false-alarm ratio and the same critical success index (see Fig. A9).

3.2.2 Effects of dynamic downscaling with original bathymetry on flood depths

Figure 10 panels d, i, n show that the model configuration N1 results in significant changes in the flood depths for all the case studies. For TC Irma (Fig. 10 panel d), model configuration N1 leads to slightly higher water levels in comparison to G1. Consequently, the resulting flood depths are also larger and are more than 0.2 m above those of G1. Maximum water levels for TC Haiyan (Fig. 10 panel i) are generally higher along the bay of Tacloban when applying dynamic downscaling with the original bathymetry. This results on average in higher flood depths of more than 1 m compared to G1. Finally, ETC Xynthia (Fig. 10 panel n) presents lower water levels for N1 compared to G1. Those lower water levels lead to lower flood depths across the whole model domain. For ETC Xynthia, N1 shows a lower hit rate and false-alarm ratio compared to G1, and the same critical success index (see Fig. A9).

3.2.3 Effects of dynamic downscaling with updated bathymetry on flood depths

Figure 10 panels e, j, o show that the model configuration N2 results in significant changes in flood depths for all case studies. For TC Irma (Fig. 10 panel e), model configuration N2 compared to G1 leads to higher and lower water levels, depending on the region. Consequently, the resulting flood depths for N2 vary between 0.05 m lower to more than 0.2 m higher than G1. Maximum water levels for TC Haiyan (Fig. 10 panel j) are generally higher in the bay of Tacloban for model configuration N2 (when applying dynamic downscaling with the updated bathymetry) compared to G1. This results in larger flood depths which, in some regions, result in more than 1 m higher compared to G1. However, in the Tacloban Bay N1 results on average in higher maximum water levels than N2, which leads to lower flood depths for N2 in comparison to N1. Finally, for ETC Xynthia (Fig. 10 panel o) water levels are lower for N2 compared to G1. Those lower water levels lead to lower flood depths across the whole model domain. For ETC Xynthia, N2 shows a lower hit rate and false-alarm ratio compared to G1, and the same critical success index (see Fig. A9).

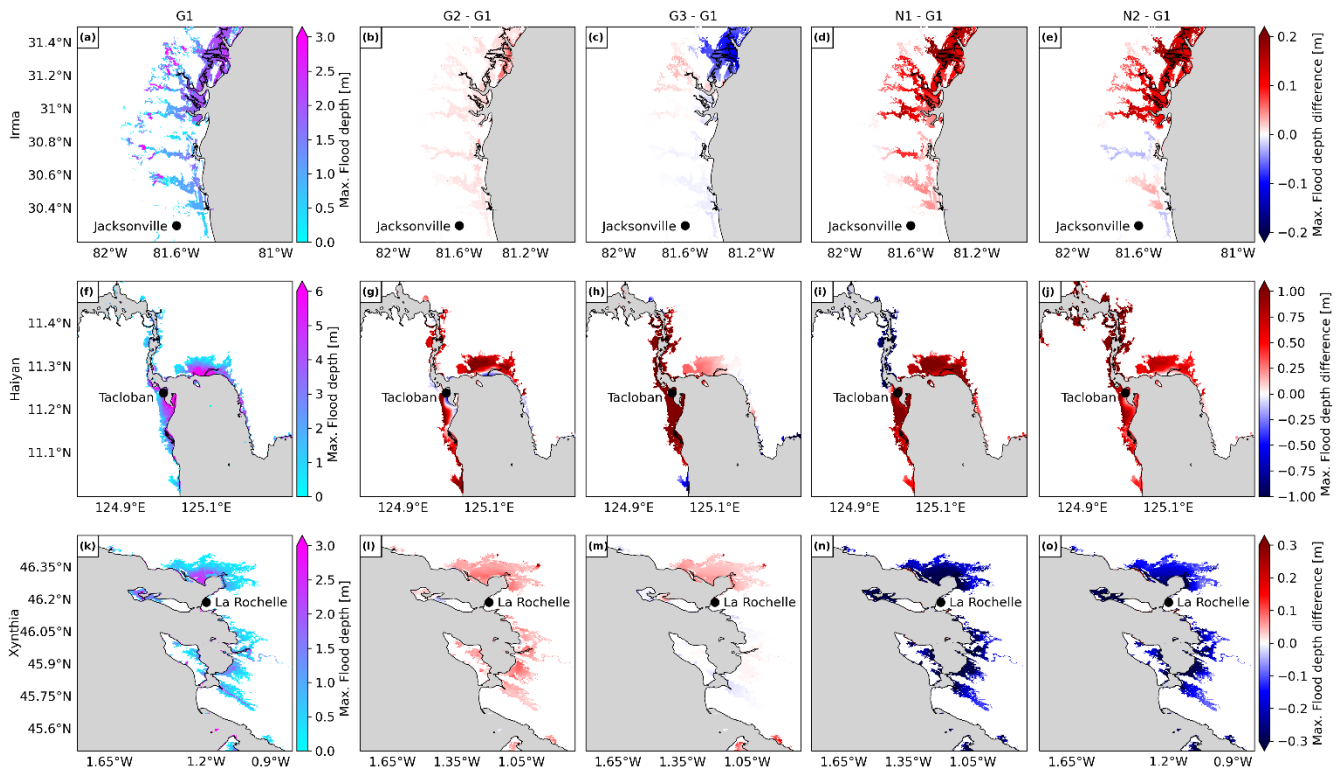
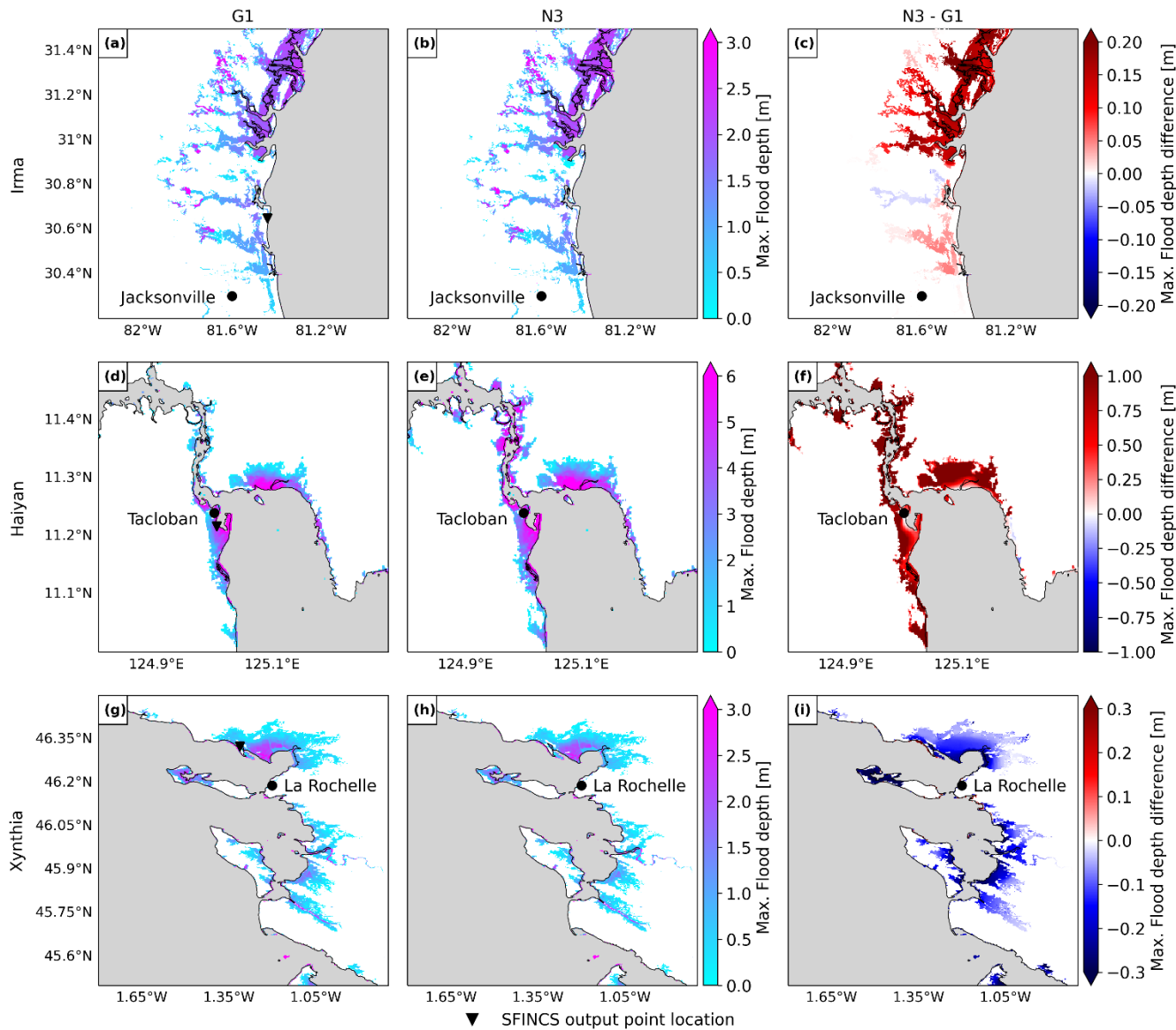


Figure 10. Panels a, f, k show the maximum flood depth for the default configuration G1, for each case study. Panels b, g, l show the difference between the maximum flood depth for the refined temporal output resolution configuration G2 and G1. Panels c, h, m show the difference between the maximum flood depth for the refined spatial output configuration G3 and G1. Panels d, i, n show the difference between the maximum flood depth for the dynamic downscaling (refined grid) configuration N1 and G1. Panels e, j, o show the difference between the maximum flood depth for the dynamic downscaling (refined grid and updated bathymetry) configuration N2 and G1.

3.2.4 Effects of a fully refined model on flood depths

For TC Irma N3 provides higher water levels throughout large parts of the domain (Section 3.1.4) that translate into higher flood depths up to more than 0.2 m near Jacksonville. For TC Haiyan, N3 provides high water levels near Tacloban (Section 3.1.4), translating into high flood depths up to more than 1 m. Finally, ETC Xynthia presents lower water levels for N3 near La Rochelle (Section 3.1.4), which translate into lower flood depths along the coast.



365

366 **Figure 11. Panels a, d, g show the maximum flood depth for the default configuration G1 for each case study. Panels b, e, h show**
367 **the maximum flood depth for the fully refined configuration N3. Panels c, f, i show the difference between the maximum flood**
368 **depth for N3 and G1.**

369 To analyse the changes of flood depths over time, Fig. 12 panels a, b, c show the flood depth timeseries at the SFINCS output
370 point locations outlined in Fig. 11, for all the model configurations. The timing and shape of the flood depth timeseries remain
371 consistent across all the model configurations for all the case studies, an only slight differences in the magnitude of the flood
372 depths are visible. Figure 12 panel a shows that for TC Irma all the model configurations result in similar flood depths, and
373 only N1 results in slightly higher flood depths of about 0.1 m more than the others. Figure 12 panel b shows that for TC Haiyan
374 G1 results in the lowest flood peak, while the temporal resolution of G2 plays a key role, enhancing the flood peak up
375 approximately 1 m higher than G1. Finally, Fig. 12 panel c shows that for all global model configurations (G1, G2 and G3)
376 result in a first flood peak that is approximately 0.5 m higher than those of the nested model configurations (N1, N2 and N3).
377 The second peak is simulated more similarly by all model configurations, being N1 the configuration that provides lowest
378 flood depths.

379 Panels a, b, c in Fig. 12 only show the results for a single SFINCS output point location. However, the refinements might have
380 most effect in other regions different than the SFINCS output point locations. To understand the overall effect of each

refinement in the flood hazard maps, Fig. 12 panels d, e, f show the flood volume timeseries across each of the case study's model domain. While the timing and shape of the flood volume timeseries remains consistent across all the model configurations for all the case studies, there are differences in the magnitude of the flood volumes. Figure 12 panel d shows that for TC Irma the nested models lead to the highest flood volumes, being N3 the model configuration that simulates the highest flood volume. On the other hand, the increase in spatial output of GTSM from G3 results in the lowest flood volumes. Figure 12 panel e shows that for TC Haiyan N3 also leads to the highest flood volumes, while G1 results in the lowest volumes. Finally, Fig. 12 panel f shows that for ETC Xynthia the nested model configurations lead to the lowest flood volumes, while the global models result in higher flood volumes.

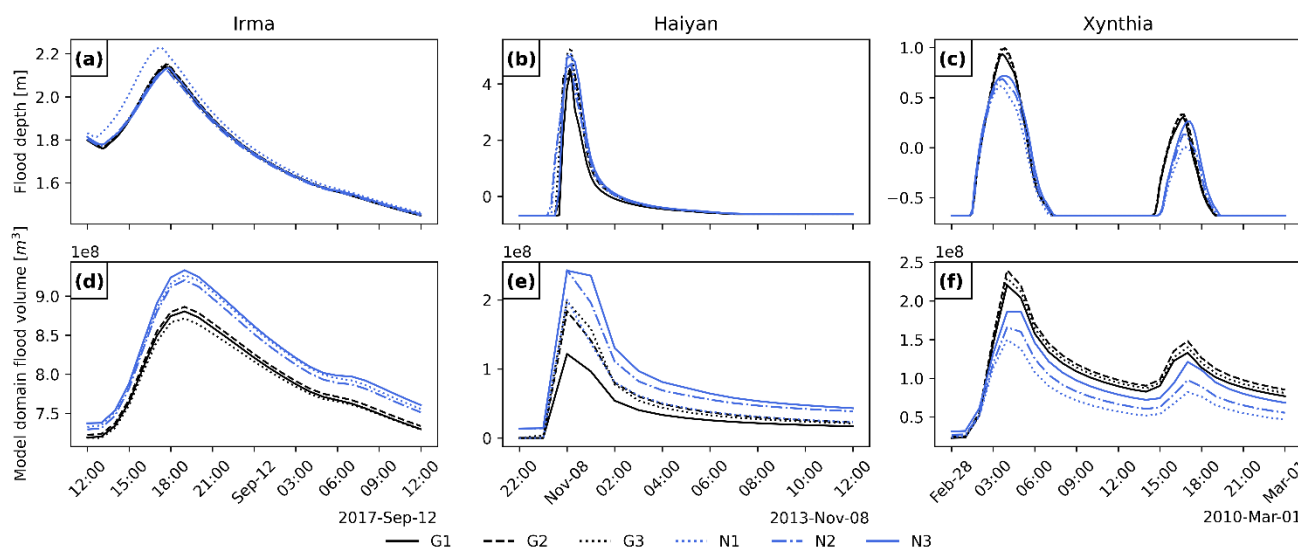


Figure 12. Flood depth timeseries for three observation points and flood volume timeseries for the SFINCS model domain of each case study and model configuration (see Table 1). The spatial location of the SFINCS output point locations can be observed in Fig. 11 panels a, d, g.

4 Discussion and Conclusions

The MOSAIC modelling framework introduced in this study allows to dynamically simulate coastal flooding events through the coupling of dynamic water level and overland flood models, making use of a Python environment. This approach is automated and reproducible, and combined with the hydrodynamic models used, makes it globally applicable. MOSAIC's flexibility allows us to easily simulate coastal flooding events globally, while also using local high-resolution models. As such, MOSAIC provides a bridge between fully global and fully local modelling approaches, and thereby paves the way for more actionable large-scale flood risk assessments.

The results of the sensitivity analysis conducted in this study reveal the complexity of hydrodynamic modelling and the sensitivity to specific local settings and storm characteristics. A comparison of the fully refined N3 configuration with the default G1 configuration reveals differing behaviours across the case studies in terms of changes in water levels and flood depths, both spatially and in magnitude. For instance, model configuration N3 simulates higher water levels almost everywhere for TC Irma. However, for TC Haiyan and ETC Xynthia, certain regions show higher water levels with N3, while others show lower water levels compared to G1. Similarly, flood depths around Jacksonville for TC Irma are generally higher with N3, although some areas experience lower values. In contrast, for TC Haiyan in Tacloban, flooding significantly increases with N3, whereas for ETC Xynthia flood depths decrease notably around La Rochelle.

Refining the temporal output resolution (model configuration G2) has a significant influence on small, rapidly intensifying TCs like Haiyan, resulting in water levels and flood depths that are 2 m and 1 m higher, respectively, compared to G1. However,

for ETCs, the refinement of temporal output resolution does not lead to substantial changes in water levels or flood depths, with a 1-hourly temporal resolution providing sufficiently accurate results. Refining the spatial output locations of GTSM (model configuration G3) provides more coastal boundary conditions for SFINCS. For regions where the water levels have more spatial heterogeneity along the coast, this refinement becomes most relevant. For TC Haiyan, for example, the coastal boundary conditions in the bay of Tacloban raised from 4 locations to more than 20 (see Fig. 7), leading to flood depths 1 m higher than G1. Furthermore, regions with more complex topographies such as the south of Florida for TC Irma or the Tacloban bay for TC Haiyan are influenced by the grid refinement of N1, leading to larger differences with G1 in terms of water levels and consequently, flooding. The choice of bathymetric datasets also plays a role in the prediction of water levels, contributing to the differences observed between N1 and N2 in all the case studies. Based on these results, we can conclude that the refinement of the global modelling approach can significantly impact the simulation of coastal water levels and flood depths at local scale, although the differences in local settings make that there is no one-size-fits-all approach.

The validation of the model configurations for the different case studies also highlights the complexities involved in refining hydrodynamic models, and how each specific setting impacts overall performance. It is challenging to assess the performance of global models due to the limited number of tide gauge stations available, meaning the validation results might not be fully representative over the entire domain. Another source of uncertainty is the location of these tide gauge stations, which are often situated in enclosed basins or harbours, where hydrodynamic models have more difficulty simulating water levels compared to open sea conditions. While the performance indicators from this study, with Pearson's correlations above 0.92 and RMSEs in general less than 0.3 m, suggest that all the refinements perform adequately and similarly to G1, the validation does not allow us to determine which model configuration consistently provides the best overall performance. This outcome largely depends on the storm characteristics and regional topography. However, the flexibility and ease of use of MOSAIC, as a Python-based framework, make it a valuable resource for users to further explore which are the optimal settings for their case study and region of interest.

There are several limitations that need to be taken into account when using MOSAIC. Limitations that are linked to general flood hazard modelling and not specific to MOSAIC include the following: (1) the meteorological forcing data can be a big source of uncertainty when modelling extreme water levels. MOSAIC allows to combine the results of the Holland model with climate reanalysis datasets in the background to enhance the wind and pressure fields at the peripheries of the TCs. Nonetheless, the implementation of more advanced wind parametric models could further improve the water level simulations (Emanuel and Rotunno, 2011; Hu et al., 2011). (2) the accuracy of the bathymetry has a large influence on storm surge modelling (Bloemendaal et al., 2019; Dullaart et al., 2020; Mori et al., 2014). When performing dynamic downscaling, MOSAIC uses bathymetry data to generate the model grid and subsequently simulate total water levels. Using higher-resolution local bathymetry enables finer grid refinement and can enhance the accuracy of the results. However, such high-resolution bathymetry is not always available. MOSAIC is set up to allow the substitution of bathymetric data with alternative datasets, to adjust the grid resolution and refinement, and to define the desired domain of the local high-resolution model. (3) digital elevation models (DEMs) can have a large influence on flood model simulations, affecting the flood hazard depth map results. In this paper we use the FABDEM's and IGN's datasets, but MOSAIC allows to replace the DEM with any dataset. In addition to the effects of DEMs, the presence of flood protection structures has substantial impact on flood hazard models. The neglect of dikes in our SFINCS model is one of the reasons our modelling framework overestimates flooding for ETC Xynthia. MOSAIC's HydroMT component supports the implementation of levees as 1D line features into the SFINCS model, and this capability could be used within MOSAIC upon the availability of flood protection data.

MOSAIC's main limitation lies in the generation of the local high-resolution models for dynamic downscaling. These automatically generated local high-resolution models can present instabilities when refined grid cells are present at the model boundaries. Therefore, care needs to be taken when applying dynamic downscaling. To solve this problem the first 0.3 degrees

around the model domain are not being refined in this study. When changes in grid refinement are abrupt, model instabilities can also occur. The nesting of multiple models in each other would allow for a smoother grid transition and might solve this issue.

In this study, we have implemented MOSAIC to simulate coastal flooding driven by storm surges. However, since flooding typically results from a combination of various drivers, our results currently underestimate flooding near estuaries and deltas due to the exclusion of precipitation and river discharge, and near steep coasts due to the exclusion of waves and overtopping. Future research on TCs and ETCs may further develop MOSAIC and include other drivers such as waves, rainfall and discharge. Considering that HydroMT and SFINCS are capable of handling compound flooding induced by pluvial and fluvial drivers (Eilander et al., 2023), there is potential for future enhancements of MOSAIC to incorporate the modelling of compound events. Furthermore, MOSAIC currently makes use of offline coupling for both the local-high resolution model and the SFINCS model. However, new software developments such as the Oceanographic Multi-purpose Software Environment (OMUSE; Pelupessy et al., 2017) could be used in the future to move from offline to online coupling, and to further expand MOSAIC by allowing for coupling with other models such as hydrological or ocean models.

Users of MOSAIC can easily simulate storm events in any region with this the modelling framework. First, they can select the appropriate meteorological forcing. Within MOSAIC, users can choose gridded meteorological data from reanalysis datasets or climate models to simulate ETCs or TCs, provided that the data accurately captures the TC wind and pressure fields (as seen with ETC Xynthia and TC Irma in this study). Alternatively, they can select a hybrid approach that combines the Holland model with ERA5 in the background when modelling smaller TCs with rapid intensification (such as TC Haiyan in this study). Depending on the specific storm simulated and study area, users can select different model refinements. For instance, the G2 model configuration with refined temporal output resolution is suitable for rapidly intensifying storms, while nested models can help resolving the topography and bathymetry in regions with complex coastlines. If the users have coastal boundary conditions available, MOSAIC can automatically generate stand-alone local high-resolution Delft3D FM models (N1, N2, and N3 model configurations) without having to couple them with GTSM. Although uncalibrated, these model configurations demonstrate similar performance than the well-established global model GTSM (G1; see Section 3), but at a significantly lower computational cost. The hydrodynamic flood modelling part of MOSAIC offers user-defined settings as well, enabling users to, for instance, choose the most suitable DEM for their study area or implement flood protection measures through MOSAIC's HydroMT component.

By leveraging the flexibility of MOSAIC to modify input datasets, the modelling framework can be used to study events under historical- and climate change conditions. Furthermore, taking advantage of MOSAIC's multiscale modelling approach, TC/ETC high-resolution hazard assessments can be obtained globally. When linked to impact models, MOSAIC can also be used for risk assessments.

Data availability

The datasets compiled and/or analysed during the current study are available on Zenodo. *Note: to be published with Doi upon acceptance of the paper.*

Code availability

The underlying code for this study is available on at https://github.com/Ireneben73/mosaic_framework (last access: 11 October 2024).

490 References

- 491 Andersen, O.B., Knudsen, P., 2009. DNSCO8 mean sea surface and mean dynamic topography models. *J. Geophys. Res.*
 492 *Oceans* 114. <https://doi.org/10.1029/2008JC005179>
- 493 Bates, P.D., Horritt, M.S., Fewtrell, T.J., 2010. A simple inertial formulation of the shallow water equations for efficient
 494 two-dimensional flood inundation modelling. *J. Hydrol.* 387, 33–45. <https://doi.org/10.1016/j.jhydrol.2010.03.027>
- 495 Bates, P.D., Quinn, N., Sampson, C., Smith, A., Wing, O., Sosa, J., Savage, J., Olcese, G., Neal, J., Schumann, G.,
 496 Giustarini, L., Coxon, G., Porter, J.R., Amodeo, M.F., Chu, Z., Lewis-Gruss, S., Freeman, N.B., Houser, T.,
 497 Delgado, M., Hamidi, A., Bolliger, I., E. McCusker, K., Emanuel, K., Ferreira, C.M., Khalid, A., Haigh, I.D.,
 498 Couasnon, A., E. Kopp, R., Hsiang, S., Krajewski, W.F., 2021. Combined Modeling of US Fluvial, Pluvial, and
 499 Coastal Flood Hazard Under Current and Future Climates. *Water Resour. Res.* 57, e2020WR028673.
 500 <https://doi.org/10.1029/2020WR028673>
- 501 Batts, M.L., Cordes, M., Russell, L., Shaver, J., Simiu, E., 1980. Hurricane Wind Speeds in the United States. *Natl. Bur.*
 502 *Stand. Build. Sci. Ser.* 106. <https://doi.org/10.1061/JSDEAG.0005541>
- 503 Bertin, X., Bruneau, N., Breilh, J.F., Fortunato, A.B., Karpitychev, M., 2012. Importance of wave age and resonance in storm
 504 surges: The case Xynthia, Bay of Biscay. *Ocean Model.* 42, 16–30. <https://doi.org/10.1016/j.ocemod.2011.11.001>
- 505 Bloemendaal, N., Muis, S., Haarsma, R.J., Verlaan, M., Irazoqui Apecechea, M., de Moel, H., Ward, P.J., Aerts, J.C.J.H.,
 506 2019. Global modeling of tropical cyclone storm surges using high-resolution forecasts. *Clim. Dyn.* 52, 5031–5044.
 507 <https://doi.org/10.1007/s00382-018-4430-x>
- 508 Breilh, J.F., Chaumillon, E., Bertin, X., Gravelle, M., 2013. Assessment of static flood modeling techniques: application to
 509 contrasting marshes flooded during Xynthia (western France). *Nat. Hazards Earth Syst. Sci.* 13, 1595–1612.
 510 <https://doi.org/10.5194/nhess-13-1595-2013>
- 511 Buchhorn, M., Smets, B., Bertels, L., Roo, B.D., Lesiv, M., Tsendbazar, N.-E., Herold, M., Fritz, S., 2020. Copernicus
 512 Global Land Service: Land Cover 100m: collection 3: epoch 2018: Globe.
 513 <https://doi.org/10.5281/ZENODO.3518038>
- 514 Bunya, S., Dietrich, J.C., Westerink, J.J., Ebersole, B.A., Smith, J.M., Atkinson, J.H., Jensen, R., Resio, D.T., Luettich, R.A.,
 515 Dawson, C., Cardone, V.J., Cox, A.T., Powell, M.D., Westerink, H.J., Roberts, H.J., 2010. A High-Resolution
 516 Coupled Riverine Flow, Tide, Wind, Wind Wave, and Storm Surge Model for Southern Louisiana and Mississippi.
 517 Part I: Model Development and Validation. <https://doi.org/10.1175/2009MWR2906.1>
- 518 Cangialosi, J.P., Latta, A.S., Berg, R., 2018. Tropical cyclone report: hurricane Irma. National Hurricane Center, Miami.
- 519 CGEDD, 2010. Tempête Xynthia: Retour d’expérience, évaluation et propositions d’action.
- 520 Consortium EMODnet Bathymetry, 2018. EMODnet Digital Bathymetry (DTM) [WWW Document]. URL
 521 <https://sextant.ifremer.fr/record/18ff0d48-b203-4a65-94a9-5fd8b0ec35f6/> (accessed 6.21.22).
- 522 DDTM, 2011. Éléments de mémoire sur la tempête Xynthia du 27 et 28 février 2010 [WWW Document]. Serv. L’État En
 523 Charente-Marit. URL <https://www.charente-maritime.gouv.fr/Actions-de-l-Etat/Environnement-risques-naturels-et-technologiques/Risques-naturels-et-technologiques/Generalites-sur-la-prevention-des-risques-naturels/Elements-de-memoire-Xynthia/Elements-de-memoire-sur-la-tempete-Xynthia-du-27-et-28-fevrier-2010> (accessed 9.16.24).
- 524 Deltares, 2024. D-Flow Flexible Mesh User Manual.
- 525 Deltares, 2021. Model description and development - Global Tide and Surge Model - Deltares Public Wiki [WWW
 526 Document]. URL <https://publicwiki.deltares.nl/display/GTSM/Model+description+and+development> (accessed
 527 10.7.24).
- 528 Dietrich, J.C., Bunya, S., Westerink, J.J., Ebersole, B.A., Smith, J.M., Atkinson, J.H., Jensen, R., Resio, D.T., Luettich, R.A.,
 529 Dawson, C., Cardone, V.J., Cox, A.T., Powell, M.D., Westerink, H.J., Roberts, H.J., 2010. A High-Resolution
 530 Coupled Riverine Flow, Tide, Wind, Wind Wave, and Storm Surge Model for Southern Louisiana and Mississippi.

Part II: Synoptic Description and Analysis of Hurricanes Katrina and Rita.

<https://doi.org/10.1175/2009MWR2907.1>

Douris, J., Kim, G., Abrahams, J., Lapitan Moreno, J., Shumake-Guillemot, J., Green, H., Murray, V., 2021. WMO Atlas of Mortality and Economic Losses from Weather, Climate and Water Extremes (1970–2019) (WMO-No. 1267), WMO. WMO, Geneva.

Dullaart, J.C.M., Muis, S., Bloemendaal, N., Aerts, J.C.J.H., 2020. Advancing global storm surge modelling using the new ERA5 climate reanalysis. *Clim. Dyn.* 54, 1007–1021. <https://doi.org/10.1007/s00382-019-05044-0>

Dullaart, J.C.M., Muis, S., Bloemendaal, N., Chertova, M.V., Couasnon, A., Aerts, J.C.J.H., 2021. Accounting for tropical cyclones more than doubles the global population exposed to low-probability coastal flooding. *Commun. Earth Environ.* 2, 1–11. <https://doi.org/10.1038/s43247-021-00204-9>

Eilander, D., Couasnon, A., Ikeuchi, H., Muis, S., Yamazaki, D., Winsemius, H.C., Ward, P.J., 2020. The effect of surge on riverine flood hazard and impact in deltas globally. *Environ. Res. Lett.* 15. <https://doi.org/10.1088/1748-9326/ab8ca6>

Eilander, D., Couasnon, A., Leijnse, T., Ikeuchi, H., Yamazaki, D., Muis, S., Dullaart, J., Haag, A., Winsemius, H.C., Ward, P.J., 2023. A globally applicable framework for compound flood hazard modeling. *Nat. Hazards Earth Syst. Sci.* 23, 823–846. <https://doi.org/10.5194/nhess-23-823-2023>

Emanuel, K., Rotunno, R., 2011. Self-Stratification of Tropical Cyclone Outflow. Part I: Implications for Storm Structure. <https://doi.org/10.1175/JAS-D-10-05024.1>

GEBCO, 2014. General Bathymetric Chart of the Oceans (GEBCO) 2014 Grid [WWW Document]. URL <https://www.gebco.net/> (accessed 6.21.22).

Haigh, I.D., Marcos, M., Talke, S.A., Woodworth, P.L., Hunter, J.R., Hague, B.S., Arns, A., Bradshaw, E., Thompson, P., 2023. GESLA Version 3: A major update to the global higher-frequency sea-level dataset. *Geosci. Data J.* 10, 293–314. <https://doi.org/10.1002/gdj3.174>

Haigh, I.D., Wadey, M.P., Wahl, T., Ozsoy, O., Nicholls, R.J., Brown, J.M., Horsburgh, K., Gouldby, B., 2016. Spatial and temporal analysis of extreme sea level and storm surge events around the coastline of the UK. *Sci. Data* 3, 1–14. <https://doi.org/10.1038/sdata.2016.107>

Harper, B.A., Kepert, J.D., Ginger, J.D., 2010. Guidelines for Converting Between Various Wind Averaging Periods in Tropical Cyclone Conditions. WMO.

Hawker, L., Uhe, P., Paulo, L., Sosa, J., Savage, J., Sampson, C., Neal, J., 2022. A 30 m global map of elevation with forests and buildings removed. *Environ. Res. Lett.* 17, 024016. <https://doi.org/10.1088/1748-9326/ac4d4f>

Hersbach, H., Bell, B., Berrisford, P., Horányi, A., Sabater, J.M., Nicolas, J., Radu, R., Schepers, D., Simmons, A., Soci, C., Dee, D., 2019. Global reanalysis: goodbye ERA-Interim, hello ERA5. *ECMWF Newsl.* 17–24. <https://doi.org/10.21957/vf291hehd7>

Hinkel, J., Lincke, D., Vafeidis, A.T., Perrette, M., Nicholls, R.J., Tol, R.S.J., Marzeion, B., Fettweis, X., Ionescu, C., Levermann, A., 2014. Coastal flood damage and adaptation costs under 21st century sea-level rise. *Proc. Natl. Acad. Sci.* 111, 3292–3297. <https://doi.org/10.1073/pnas.1222469111>

Holland, G.J., Belanger, J.I., Fritz, A., 2010. A revised model for radial profiles of hurricane winds. *Mon. Weather Rev.* 138, 4393–4401. <https://doi.org/10.1175/2010MWR3317.1>

Hu, K., Chen, Q., Kimball, S.K., 2011. Consistency in hurricane surface wind forecasting: an improved parametric model. *Nat. Hazards* 61, 1029–1050. <https://doi.org/10.1007/s11069-011-9960-z>

Kernkamp, H.W.J., Van Dam, A., Stelling, G.S., de Goede, E.D., 2011. Efficient scheme for the shallow water equations on unstructured grids with application to the Continental Shelf. *Ocean Dyn.* 61, 1175–1188. <https://doi.org/10.1007/s10236-011-0423-6>

576 Kirezci, E., Young, I.R., Ranasinghe, R., Muis, S., Nicholls, R.J., Lincke, D., Hinkel, J., 2020. Projections of global-scale
577 extreme sea levels and resulting episodic coastal flooding over the 21st Century. *Sci. Rep.* 10, 1–12.
578 <https://doi.org/10.1038/s41598-020-67736-6>

579 Lapidez, J.P., Tablazon, J., Dasallas, L., Gonzalo, L.A., Cabacaba, K.M., Ramos, M.M.A., Suarez, J.K., Santiago, J.,
580 Lagmay, A.M.F., Malano, V., 2015. Identification of storm surge vulnerable areas in the Philippines through the
581 simulation of Typhoon Haiyan-induced storm surge levels over historical storm tracks. *Hazards Earth Syst Sci* 15,
582 1473–1481. <https://doi.org/10.5194/nhess-15-1473-2015>

583 Leijnse, T., Nederhoff, K., Van Dongeren, A., McCall, R.T., Van Ormondt, M., 2020. Improving Computational Efficiency
584 of Compound Flooding Simulations: the SFINCS Model with Subgrid Features 2020, NH022-0006.

585 Leijnse, T., Van Ormondt, M., Nederhoff, K., Van Dongeren, A., 2021. Modeling compound flooding in coastal systems
586 using a computationally efficient reduced-physics solver: Including fluvial, pluvial, tidal, wind- and wave-driven
587 processes. *Coast. Eng.* 163, 103796. <https://doi.org/10.1016/j.coastaleng.2020.103796>

588 Lin, N., Chavas, D., 2012. On hurricane parametric wind and applications in storm surge modeling. *J. Geophys. Res.*
589 *Atmospheres* 117, 1–19. <https://doi.org/10.1029/2011JD017126>

590 Marcos, M., Rohmer, J., Vousedoukas, M.I., Mentaschi, L., Le Cozannet, G., Amores, A., 2019. Increased Extreme Coastal
591 Water Levels Due to the Combined Action of Storm Surges and Wind Waves. *Geophys. Res. Lett.* 46, 4356–4364.
592 <https://doi.org/10.1029/2019GL082599>

593 Mori, N., Kato, M., Kim, S., Mase, H., Shibutani, Y., Takemi, T., Tsuboki, K., Yasuda, T., 2014. Local amplification of
594 storm surge by Super Typhoon Haiyan in Leyte Gulf. *Geophys. Res. Lett.* 41, 5106–5113.
595 <https://doi.org/10.1002/2014GL060689>

596 Muis, S., Apecechea, M.I., Dullaart, J., de Lima Rego, J., Madsen, K.S., Su, J., Yan, K., Verlaan, M., 2020. A High -
597 Resolution Global Dataset of Extreme Sea Levels, Tides, and Storm Surges, Including Future Projections. *Front.*
598 *Mar. Sci.* 7, 1–15. <https://doi.org/10.3389/fmars.2020.00263>

599 Muis, S., Verlaan, M., Winsemius, H.C., Aerts, J.C.J.H., Ward, P.J., 2016. A global reanalysis of storm surges and extreme
600 sea levels. *Nat. Commun.* 7, 11969. <https://doi.org/10.1038/ncomms11969>

601 Naval Meteorology and Oceanography Command, 2022. Naval Oceanography Portal, Best Track Archive [WWW
602 Document]. URL <https://www.metoc.navy.mil/jtwc/jtwc.html?best-tracks> (accessed 10.10.24).

603 Nhamo, G., Chikodzi, D., 2021. Cyclones in Southern Africa: Volume 1: Interfacing the Catastrophic Impact of Cyclone Idai
604 with SDGs in Zimbabwe, Sustainable Development Goals Series. Springer International Publishing, Cham.
605 <https://doi.org/10.1007/978-3-030-72393-4>

606 Pelupessy, I., Van Werkhoven, B., Van Elteren, A., Viebahn, J., Candy, A., Zwart, S.P., Dijkstra, H., 2017. The
607 Oceanographic Multipurpose Software Environment (OMUSE v1.0). *Geosci. Model Dev.* 10, 3167–3187.
608 <https://doi.org/10.5194/gmd-10-3167-2017>

609 Pringle, W.J., Wirasaet, D., Roberts, K.J., Westerink, J.J., 2021. Global storm tide modeling with ADCIRC v55:
610 unstructured mesh design and performance. *Geosci. Model Dev.* 14, 1125–1145. <https://doi.org/10.5194/gmd-14-1125-2021>

611

612 Ramirez, J.A., Lichter, M., Coulthard, T.J., Skinner, C., 2016. Hyper-resolution mapping of regional storm surge and tide
613 flooding: comparison of static and dynamic models. *Nat. Hazards* 82, 571–590. <https://doi.org/10.1007/s11069-016-2198-z>

614

615 Sebastian, A., Bader, D.J., Nederhoff, C.M., Leijnse, T.W.B., Bricker, J.D., Aarninkhof, S.G.J., 2021. Hindcast of pluvial,
616 fluvial, and coastal flood damage in Houston, Texas during Hurricane Harvey (2017) using SFINCS. *Nat. Hazards*.
617 <https://doi.org/10.1007/s11069-021-04922-3>

618 Tiggeloven, T., De Moel, H., Winsemius, H.C., Eilander, D., Erkens, G., Gebremedhin, E., Diaz Loaiza, A., Kuzma, S., Luo,
 619 T., Iceland, C., Bouwman, A., Van Huijstee, J., Ligtoet, W., Ward, P.J., 2020. Global-scale benefit-cost analysis of
 620 coastal flood adaptation to different flood risk drivers using structural measures. *Nat. Hazards Earth Syst. Sci.* 20,
 621 1025–1044. <https://doi.org/10.5194/nhess-20-1025-2020>
 622 UNDRR, 2020. The human cost of disasters: an overview of the last 20 years (2000–2019) | UNDRR [WWW Document].
 623 URL <https://www.undrr.org/publication/human-cost-disasters-overview-last-20-years-2000-2019> (accessed
 624 9.27.22).
 625 Vafeidis, A.T., Schuerch, M., Wolff, C., Spencer, T., Merkens, J.L., Hinkel, J., Lincke, D., Brown, S., Nicholls, R.J., 2019.
 626 Water-level attenuation in global-scale assessments of exposure to coastal flooding: A sensitivity analysis. *Nat.*
 627 *Hazards Earth Syst. Sci.* 19, 973–984. <https://doi.org/10.5194/nhess-19-973-2019>
 628 Veenstra, J., 2024. dfm_tools: A Python package for pre- and postprocessing D-FlowFM model input and output files.
 629 <https://doi.org/10.5281/zenodo.10633862>
 630 Vitousek, S., Barnard, P.L., Fletcher, C.H., Frazer, N., Erikson, L., Storlazzi, C.D., 2017. Doubling of coastal flooding
 631 frequency within decades due to sea-level rise. *Sci. Rep.* 7, 1–9. <https://doi.org/10.1038/s41598-017-01362-7>
 632 Vousdoukas, M.I., Bouziotas, D., Giardino, A., Bouwer, L.M., Mentaschi, L., Voukouvalas, E., Feyen, L., 2018a.
 633 Understanding epistemic uncertainty in large-scale coastal flood risk assessment for present and future climates.
 634 *Nat. Hazards Earth Syst. Sci.* 18, 2127–2142. <https://doi.org/10.5194/nhess-18-2127-2018>
 635 Vousdoukas, M.I., Mentaschi, L., Voukouvalas, E., Verlaan, M., Feyen, L., 2017. Extreme sea levels on the rise along
 636 Europe’s coasts. *Earths Future* 5, 304–323. <https://doi.org/10.1002/2016EF000505>
 637 Vousdoukas, M.I., Mentaschi, L., Voukouvalas, E., Verlaan, M., Jevrejeva, S., Jackson, L.P., Feyen, L., 2018b. Global
 638 probabilistic projections of extreme sea levels show intensification of coastal flood hazard. *Nat. Commun.* 9, 1–12.
 639 <https://doi.org/10.1038/s41467-018-04692-w>
 640 Vousdoukas, M.I., Voukouvalas, E., Annunziato, A., Giardino, A., Feyen, L., 2016a. Projections of extreme storm surge
 641 levels along Europe. *Clim. Dyn.* 47, 3171–3190. <https://doi.org/10.1007/s00382-016-3019-5>
 642 Vousdoukas, M.I., Voukouvalas, E., Mentaschi, L., Dottori, F., Giardino, A., Bouziotas, D., Bianchi, A., Salamon, P., Feyen,
 643 L., 2016b. Developments in large-scale coastal flood hazard mapping. *Nat. Hazards Earth Syst. Sci.* 16, 1841–1853.
 644 <https://doi.org/10.5194/nhess-16-1841-2016>
 645 Wadey, M.P., Haigh, I.D., Nicholls, R.J., Brown, J.M., Horsburgh, K., Carroll, B., Gallop, S.L., Mason, T., Bradshaw, E.,
 646 2015. A comparison of the 31 January–1 February 1953 and 5–6 December 2013 coastal flood events around the
 647 UK. *Front. Mar. Sci.* 2. <https://doi.org/10.3389/fmars.2015.00084>
 648 Wahl, T., 2017. Sea-level rise and storm surges, relationship status: Complicated! *Environ. Res. Lett.* 12.
 649 <https://doi.org/10.1088/1748-9326/aa8eba>
 650 Wahl, T., Haigh, I.D., Nicholls, R.J., Arns, A., Dangendorf, S., Hinkel, J., Slangen, A.B.A., 2017. Understanding extreme
 651 sea levels for broad-scale coastal impact and adaptation analysis. *Nat. Commun.* 8, 1–12.
 652 <https://doi.org/10.1038/ncomms16075>
 653 Wang, P., Bernier, N.B., 2023. Adding sea ice effects to a global operational model (NEMO v3.6) for forecasting total water
 654 level: approach and impact. *Geosci. Model Dev.* 16, 3335–3354. <https://doi.org/10.5194/gmd-16-3335-2023>
 655 Wang, X., Verlaan, M., Apecechea, M.I., Lin, H.X., 2022. Parameter estimation for a global tide and surge model with a
 656 memory-efficient order reduction approach. *Ocean Model.* 173, 102011.
 657 <https://doi.org/10.1016/j.ocemod.2022.102011>
 658 Ward, P.J., Blauhut, V., Bloemendaal, N., Daniell, E.J., De Ruiter, C.M., Duncan, J.M., Emberson, R., Jenkins, F.S.,
 659 Kirschbaum, D., Kunz, M., Mohr, S., Muis, S., Riddell, A.G., Schäfer, A., Stanley, T., Veldkamp, I.E.T., Hessel,

W.C., 2020. Review article: Natural hazard risk assessments at the global scale. *Nat. Hazards Earth Syst. Sci.* 20, 1069–1096. <https://doi.org/10.5194/nhess-20-1069-2020>

Weatherall, P., Tozer, B., Arndt, J.E., Bazhenova, E., Bringensparr, C., Castro, C., Dorschel, B., Ferrini, V., Hehemann, L., Jakobsson, M., Johnson, P., Ketter, T., Mackay, K., Martin, T., McMichael-Phillips, J., Mohammad, R., Nitsche, F., Sandwell, D., Viquerat, S., 2020. The GEBCO_2020 Grid - a continuous terrain model of the global oceans and land. <https://doi.org/10.5285/a29c5465-b138-234d-e053-6c86abc040b9>

Woodruff, J., Dietrich, J.C., Wirasaet, D., Kennedy, A.B., Bolster, D., 2023. Storm surge predictions from ocean to subgrid scales. *Nat. Hazards* 117, 2989–3019. <https://doi.org/10.1007/s11069-023-05975-2>

Acknowledgements

This work was carried out in the EU-ERC COASTMOVE project nr 884442 and the NWO MOSAIC project nr ASDI.2018.036. The authors would like to thank the SURF Cooperative for the support in using the Dutch national e-infrastructure under grant no. EINF-2224 and EINF-5779.

Author contributions

I.B.: Conceptualisation, Investigation, Methodology, Modelling, Visualisation, Analysis, Writing – Original Draft. J.C.J.H.A.: Conceptualisation, Investigation, Methodology, Writing – Review & Editing, Supervision. P.J.W.: Conceptualisation, Investigation, Methodology, Writing – Review & Editing, Supervision. D.E.: Conceptualisation, Investigation, Methodology, Modelling, Writing – Review & Editing, Supervision. S.M.: Conceptualisation, Investigation, Methodology, Modelling, Writing – Review & Editing, Supervision.

Competing interests

One of the (co-)authors is a member of the editorial board of *Natural Hazards and Earth System Sciences*.